Energy & Environmental Science

ROYAL SOCIETY OF CHEMISTRY

PAPER

View Article Online
View Journal

Check for updates

Cite this: DOI: 10.1039/d5ee01597a

Blocking pore design enables highly reversible lithium–chlorine batteries†

Junwei Han, ‡[ad] Xinru Wei,‡[b] Guanzhong Ma,[b] Han Wang,[d] Yiming Sun,[b] Zihui Liu,[b] Lu Zhao,[e] Chenyu Ma,[b] Qihao Liu,[d] Wenting Feng,[d] Debin Kong, *[b] Wei Lv, [f] Quan-Hong Yang *[c] and Linjie Zhi *[ab]

Received 21st March 2025,
Accepted 8th July 2025

DOI: 10.1039/d5ee01597a

rsc.li/ees

Rechargeable lithium–chlorine (Li–Cl_2) batteries are recognized as powerful candidates for energy storage due to high energy density and adaptability in harsh environments. However, porous materials used in Li–Cl_2 battery cathodes exhibit poor confinement of active chlorine species, which significantly challenges the rechargeability of batteries. Herein, we propose a blocking pore design to enable strong confinement and highly reversible conversion of chlorine species, where a narrow pore-entrance blocking effect confines LiCl growth in the pore body and suppresses Cl_2 spillage from the pores. As a result, the obtained Li–Cl_2 battery demonstrates a high gravimetric capacity of 3863 mAh g^{-1}, along with a super-long cycle life (750 cycles) and remarkable rate capability (616 mAh g^{-1} at 30 A g^{-1}). This work presents a novel chlorine confinement mechanism to improve the reversibility of chlorine conversion in metal-chlorine batteries.

Broader context

Rechargeable lithium–chlorine (Li–Cl_2) batteries play a vital role in cutting-edge energy storage systems due to their high output voltage (~3.5 V), potentially high energy density (~700 Wh kg^{-1}), and excellent environmental adaptability. However, the sluggish chlorine conversion still limits the development of Li–Cl_2 batteries. Although the reaction kinetics of Li–Cl_2 batteries can be improved by providing physical or chemical actions, their applications are still challenged by the low pore utilization ratio to achieve strong LiCl and Cl_2 confinement simultaneously. Herein, we present a pore design rationale for the Li–Cl_2 battery cathode host by effectively integrating the strong chlorine confinement to afford nanopore-confined chlorine conversion. This rationale is successfully achieved through a blocking pore design with a narrow pore neck and large pore body, featuring a pore-entrance block effect that enables strong confinement and highly reversible conversion of active chlorine species.

Introduction

Rechargeable lithium–chlorine (Li–Cl_2) batteries have high theoretical energy density (710 Wh kg^{-1}) and excellent adaptability across a wide temperature range, demonstrating great potential for use in harsh environments.[1–7] The Li–Cl_2 battery operates through an initial irreversible discharge of thionyl chloride ($SOCl_2$) to produce lithium chloride (LiCl) as the active material, which initiates the subsequent reversible electrochemical conversion between LiCl and Cl_2.[1,8–12] Dai *et al.* reported a rechargeable Li–Cl_2 battery derived from primary $SOCl_2$ chemistry, which broke the non-rechargeable characteristics of Li–$SOCl_2$ batteries for the first time.[1,11] In this new battery configuration, the use of porous carbon with high electrical conductivity and a high specific surface area as a cathode host is crucial, as it accommodates the discharged product LiCl and contains the charged product Cl_2, thereby promoting their reversible conversion.[1,6,13–15] Nevertheless, the

[a] Research Center on Advanced Chemical Engineering and Energy Materials, China University of Petroleum (East China), 266580, China. E-mail: zhilj@upc.edu.cn
[b] Shandong Key Laboratory of Advanced Electrochemical Energy Storage Technologies, College of New Energy, China University of Petroleum (East China), 266580, China. E-mail: kongdb@upc.edu.cn
[c] Nanoyang Group, Tianjin Key Laboratory of Advanced Carbon and Electrochemical Energy Storage, State Key Laboratory of Chemical Engineering, School of Chemical Engineering and Technology, Tianjin University, Tianjin 300072, China. E-mail: qhyangcn@tju.edu.cn
[d] School of Materials Science and Engineering, China University of Petroleum (East China), 266580, China
[e] College of Chemistry and Chemical Engineering, China University of Petroleum (East China), Qingdao 266580, China
[f] Shenzhen Geim Graphene Center, Tsinghua Shenzhen International Graduate School, Tsinghua University, Shenzhen, 518055, China

† Electronic supplementary information (ESI) available. See DOI: https://doi.org/10.1039/d5ee01597a

‡ These authors contributed equally.

Published on 14 July 2025. Downloaded by Yunnan University on 8/3/2025 3:58:32 PM.

Published on 14 July 2025. Downloaded by Yunnan University on 8/3/2025 3:58:32 PM.

conversion polarizations between LiCl and Cl_2 remain significant owing to LiCl aggregation or Cl_2 spillage, which leads to the short cycle life ($\sim$100 cycles), low gravimetric capacity ($<$1000 mAh g^{-1}, calculated based on the porous host) and the small charging current density ($\leq$2 A g^{-1}) of current Li–Cl_2 batteries.

To further improve chlorine conversion efficiency, several pioneering research works have been devoted mainly to developing new porous cathode host materials, including defective graphite,[13] heteroatom-doped bicontinuous-structured carbon,[16] imine-functionalized porous organic nanocage,[3] amine-functionalized covalent organic framework,[17] and porous metal–organic frameworks (MOF).[18] The application of these carefully selected porous cathode hosts could alleviate LiCl aggregation and Cl_2 diffusion, delivering improved chlorine reversibility. Nevertheless, in current Li–Cl_2 batteries, the chlorine conversion efficiency and pore utilization remain low, resulting in a significant gap from practical application in terms of specific capacity, cyclic stability, and rate performance. Recently, Chen *et al.* pointed out that the distribution of the discharge products of metal chloride on the cathode and the chlorine confinement ability are strongly related to the pore structure of cathode materials, which significantly impacts the rechargeability of Li–Cl_2 batteries.[6] However, when using these conventional porous host materials in Li–Cl_2 batteries, high specific surface areas, large pore volume, and appropriate surficial chemistry are commonly concerning,[1,18–22] but until now, the factor of pore configuration has not been emphasized, which directly determines the pore confinement strength on the chlorine species and their conversion efficiencies.

The used cathode host always presents pores with open micropores to effectively trap Cl_2 upon reversible charging;[1,6] however, the small microporous pores below 2 nm have difficulty in efficiently distributing the LiCl deposited upon the initial discharging, demonstrating inferior LiCl confinement performance and easily causing large LiCl particle agglomeration and passivation outside the pores (in the second quadrant of Fig. 1). In addition, the large open mesopores or macropores with sufficient void space offer advantages in accommodating and distributing the deposited LiCl upon discharging.[16] However, they unavoidably cause easy escaping and shuttling of Cl_2 owing to the open pore entrance, presenting unsatisfactory capacity and inferior cycling performance (in the fourth quadrant of Fig. 1). The pores with a relatively closed structure ($<$0.5 nm) potentially have strong confinement for both LiCl and Cl_2.[23] However, the LiCl produced in the first discharging process cannot be deposited into it owing to the isolation of the electrolyte outside of the pore, resulting in a low pore utilization ratio (in the third quadrant of Fig. 1). Therefore, to address the poor chlorine confinement resulting from the dilemma of accommodating LiCl in large pores and trapping Cl_2 in small pores for the Li–Cl_2 battery cathode host, new chlorine confinement modes are highly desired.

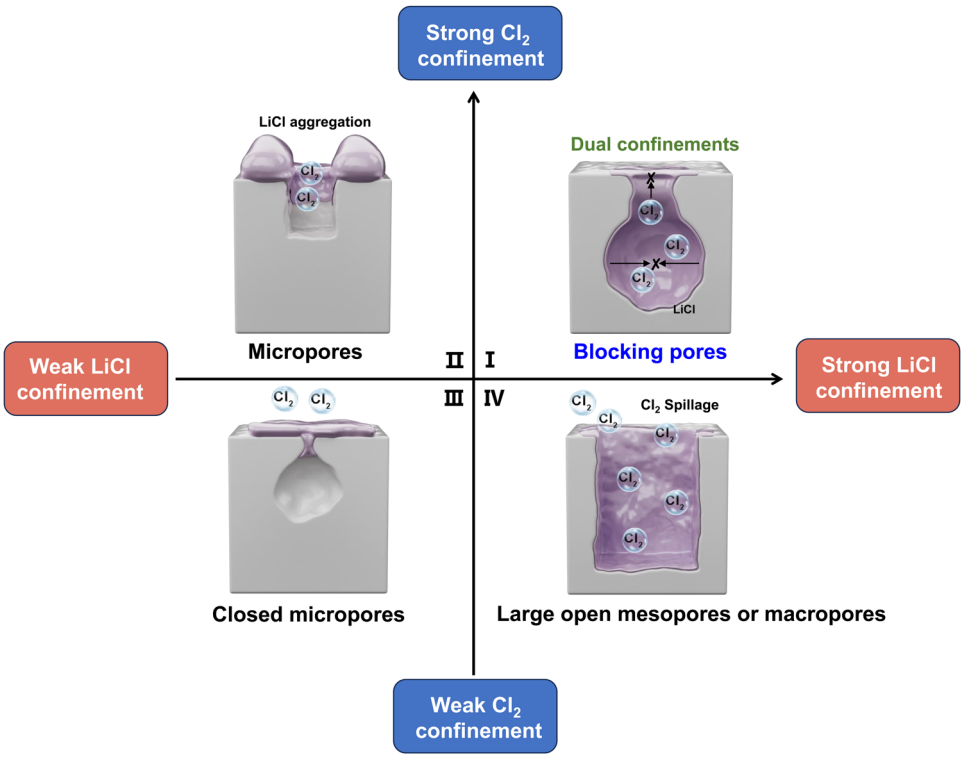

Fig. 1 Schematic of the blocking pore design for chlorine confinement. (I) Blocking pore design achieves dual confinement of LiCl and Cl_2 inside the nanopores through a narrow pore-entrance blocking effect. (II) The most used open-micropore carbon in the rechargeable metal–Cl_2 battery cathode. (III) For closed micropores with very tightened pore entrances, the theoretical Cl_2 trapping ability is the strongest; however, in reality, the LiCl initially faces a considerable difficulty in depositing into these tightened pores. (IV) Large open mesopores or macropores in carbon supports provide sufficient space for uniform LiCl deposition; however, their large open pore entrances have an weak effect on Cl_2 confinement.

This journal is © The Royal Society of Chemistry 2025

Published on 14 July 2025. Downloaded by Yunnan University on 8/3/2025 3:58:32 PM.

In this work, we proposed a blocking pore design for the Li–Cl_2 battery cathode to achieve strong confinement and highly reversible conversion of chlorine species (in the first quadrant of Fig. 1). This blocking pore features a narrow pore entrance (~3.8 nm) and large pore body (~5–16 nm), enabling a pore-entrance blocking effect to trap both LiCl and Cl_2 in the pores, where fine lithium chloride (LiCl) particles are deposited in pores and without aggregation outside the pores upon discharging and the chlorine (Cl_2) is suppressed without spillage out of pores upon charging (Fig. 2A). The density functional

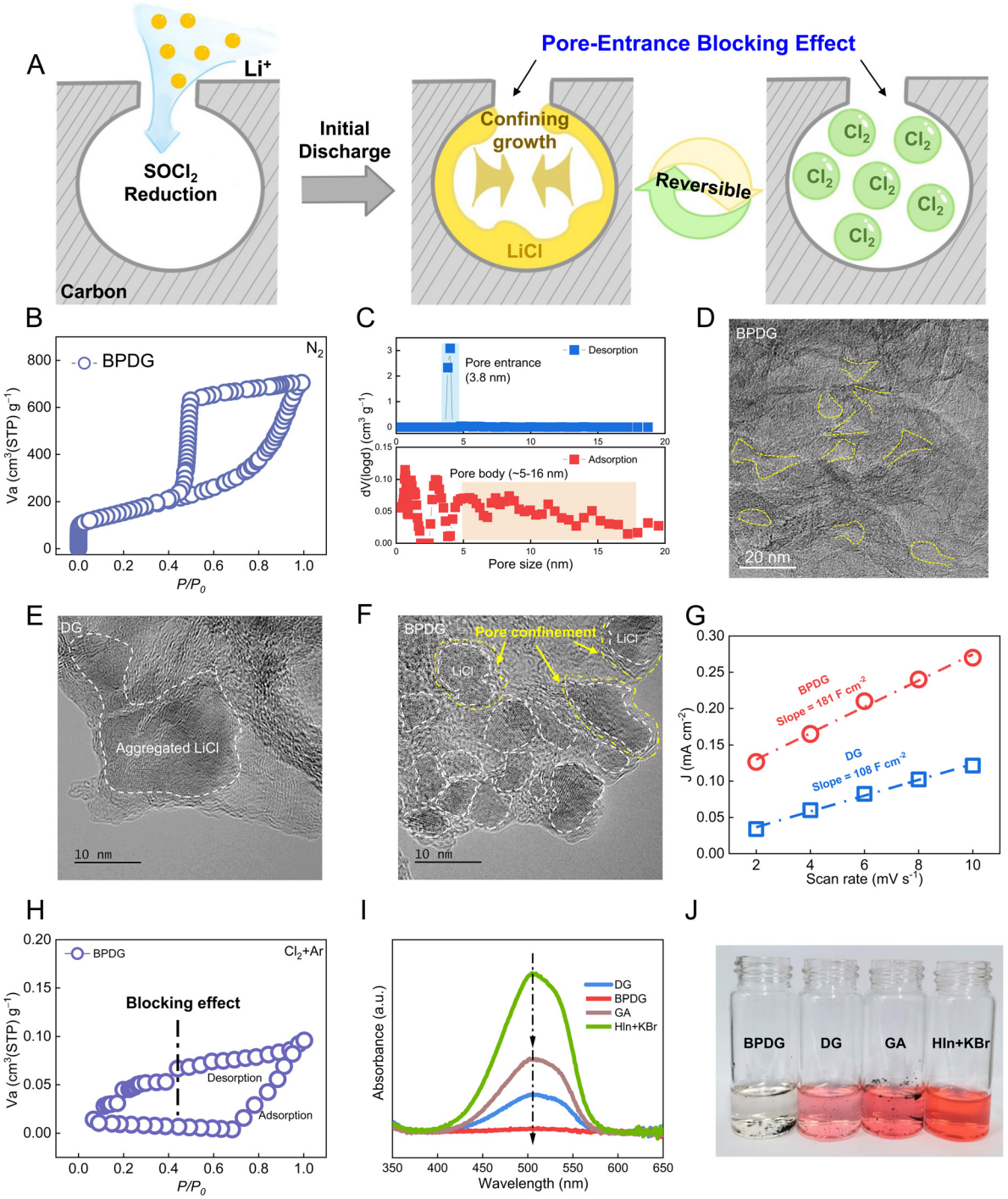

Fig. 2 Characterizations of blocking-pore confinements of LiCl and Cl_2. (A) Schematic of the blocking pores achieving strong confinement and highly reversible conversion of LiCl and Cl_2. (B) N_2 adsorption–desorption isotherms of BPDG. (C) Pore entrance and pore body size analysis for BPDG. (D) High-resolution TEM image of BPDG. (E) and (F) HRTEM image of LiCl deposited in (E) DG and (F) BPDG. (G) Calculated electrochemical surface area comparison for BPDG and DG. (H) Cl_2 and Ar mixture adsorption–desorption isotherms of BPDG. (I) UV-vis spectroscopy of Cl_2 trapping content in the BPDG, DG, and GA and (J) the corresponding color change photo of HIn + KBr solution.

Published on 14 July 2025. Downloaded by Yunnan University on 8/3/2025 3:58:32 PM.

theory (DFT) calculation combined with the electrochemical analysis proves that the achieved chlorine confinement in blocking pores delivers much higher reaction efficiency than that of micropores and larger pores, achieving an ultrahigh gravimetric capacity of 3863 mAh g^{-1} for Li–Cl_2 batteries (all the specific capacities are calculated on the mass of porous carbon[1,3,5]). Moreover, the significantly enhanced chlorine conversion kinetics delivers a long battery cycle life (750 cycles, 1.5 times longer than the previously longest cycle life among Li–Cl_2 batteries) and remarkable rate capability (616 mAh g^{-1} at 30 A g^{-1}, 6 times higher than the previous highest reported current density of 5 A g^{-1} for ~500 mAh g^{-1} among Li–Cl_2 batteries). The obtained Li–Cl_2 batteries also demonstrate excellent cycling performance at low temperatures (−40 °C) and in lean electrolytes (60 μL), which robustly confirms the effectiveness of the blocking pore for chlorine conversion under practical conditions.

Results and discussion

Dual confinements of LiCl and Cl_2 enabled by blocking pores

The blocking pores were formed in a densely assembled three-dimensional (3D) graphene network through the capillary shrinkage of graphene hydrogel and H_3PO_4 activation.[24] Specifically, a graphene hydrogel was first prepared by the self-assembling gelation of graphene oxide (GO) under hydrothermal conditions (180 °C).[25] In this process, the graphene oxide was partially thermally reduced, resulting in the removal of some –COOH or –OH functional groups. As for the formation of the 3D graphene network in this graphene hydrogel, the graphene assembly process begins with the phase separation of GO, which enables the formation of a 3D interconnected structure, and water acts as the spacer, preventing the stacking of graphene nanosheets and helping to produce a networked pore structure.[25] The fabricated reduced graphene oxide (rGO) hydrogel would be treated with evaporation-induced capillary drying and subjected to capillary shrinkage by capillary force pulling the network, which differs from freeze-drying, which retains the graphene network without shrinkage. After a typical evaporation-induced capillary drying of the graphene hydrogel, large pores formed by the 3D interconnected graphenes would shrink into interconnected small pores due to the capillary force induced by the removed water pulling the graphene network to contract upon drying (~100 × volume shrinkage, Fig. S1, ESI†).[26–28] When this reduced graphene oxide (rGO) hydrogel was treated with H_3PO_4 infiltration through sufficient static adsorption, capillary drying was used to achieve the rGO hydrogel shrinkage. After further heating at 600 °C,[29,30] this shrunk dense graphene assembly with abundant blocking pores (BPDG) was obtained. In this fabrication process, the cross-linking interactions between H_3PO_4 clusters (H_3PO_4 molecules combined by hydrogen bonds) and graphene nanosheets provide support between the shrinking graphene network, together with a further chemical reaction, which finally generates interconnected mesopores with wide pore bodies and narrow pore entrances.[24,31–33] As a control sample, the dense graphene assembly (DG) was fabricated using a capillary–shrunk graphene hydrogel and heat treatment, without H_3PO_4 activation, which resulted in a larger shrinkage degree with main interconnected micropores and a few small mesopores.

Scanning electron microscopy (SEM) was first used to observe the microstructure of BPDG and DG. As shown in Fig. S2A and B (ESI†), both BPDG and DG show densely networked graphene with interconnected porous structures. The major difference between these two samples is that BPDG exhibits more developed pores than DG. Their pore structure information was investigated by the N_2 adsorption–desorption isotherms at 77 K. As shown in Fig. 2B and Fig. S2C (ESI†), both type I and IV isotherms are demonstrated in BPDG and DG, illustrating the typical micro- and meso-pores. Notably, BPDG has a much larger hysteresis loop at a relative pressure above 0.4 than that of DG, implying a main mesopore structure in BPDG. More importantly, the desorption branch shows an obvious type of H2a hysteresis hoop.[24,34] This type of pore structure has a typical blocking effect, where the desorption of N_2 filled in the wide pore body is hindered by the narrow pore entrance until the relative pressure decreases below 0.4. Before approaching this low relative pressure, the pore body remains filled with the adsorbed N_2.[34] By analyzing the adsorption and desorption branches, the pore body has a main size of ~5–16 nm, and the pore entrance size is ~3.8 nm (Fig. 2C). The volume ratio of the blocking pores is ~83% of the total pore volume, calculated by the pore volume of blocking pores (0.88 cm^3 g^{-1}) divided by the total pore volume (1.06 cm^3 g^{-1}) obtained from the accumulated pore size distribution curves in Fig. S3 (ESI†). By contrast, DG shows a much smaller hysteresis loop and depressed desorption branch with a weak pore block effect on N_2 escaping (Fig. S2C, ESI†), and the main pore structure is the interconnected micropores (<2 nm, Fig. S4, ESI†) produced by the full contraction of the graphene hydrogel due to the absence of the H_3PO_4 cluster supporting the shrinking graphene sheets. The micropore volume is ~57% of the total pore volume for DG, in contrast with the ~9% micropores in BPDG. High-resolution transmission electron microscopy (HRTEM) characterization was conducted to directly observe the pore structure of BPDG and DG, as shown in Fig. 2D and Fig. S2D (ESI†). Due to the full shrinkage of the graphene network, the micropores or small mesopores are present in DG. For comparison, many pores with large pore bodies and tightened pore entrances were detected in BPDG (Fig. 2D), consistent with the N_2 adsorption–desorption results.

From the analysis of N_2 adsorption and desorption, the N_2 would be confined by the narrow pore entrance when it was filled into the pore body after adsorption, which causes the N_2 to have difficulty escaping from the pores due to the narrow pore-entrance blocking effect. Therefore, this kind of pore could be potentially used to confine chlorine species in Li–Cl_2 batteries. The adsorption and desorption experiment of Cl_2 (mixing Ar with 95% in volume for safety and using an anti-corrosion device under 298 K) in BPDG also obviously demonstrates the blocking effect similar to this Cl_2/Ar mixed gas

 This journal is © The Royal Society of Chemistry 2025

Published on 14 July 2025. Downloaded by Yunnan University on 8/3/2025 3:58:32 PM.

adsorption and desorption, where the adsorbed Cl_2 in these pores cannot escape the pore until the relative pressure decreases below 0.4 (Fig. 2H). For comparison, the sloped desorption curve without effective gas containment when the pressure decreased for other micropores (typically YP80F[35,36]) and mesoporous carbons (typically CMK-3) illustrates a very weak pore-entrance blocking effect during desorption (Fig. S5, ESI†). Therefore, the blocking pore with a large pore body and narrow pore entrance holds the potential to confine LiCl particle growth without aggregation outside the pores upon discharge, and subsequently, could confine the produced Cl_2 within the pores without spillage upon charging.

We investigated the effectiveness of blocking pores for LiCl and the Cl_2 confinements in BPDG. Firstly, Li–Cl_2 batteries were assembled using BPDG or DG as the cathode host, metallic Li as the anode, $SOCl_2$ with 4 M aluminum chloride ($AlCl_3$), 2 wt% lithium trifluoromethanesulfonimide (LiTFSI) and 2 wt% lithium bis(fluorosulfonyl)imide (LiFSI) additives as electrolytes. In this experiment, the mass loading of DG with a lower pore volume per gram (0.27 $cm^3\ g^{-1}$) was increased to obtain an equal total pore volume to that of BPDG (1.07 $cm^3\ g^{-1}$) in the cathode. After an initial discharging process (to 2 V) of $SOCl_2$, reducing to LiCl with Li^+, we used HRTEM to observe the LiCl deposition in DG and BPDG. We found that LiCl has a dense and aggregated distribution on the surface of DG (Fig. 2E and Fig. S6, ESI†). In sharp contrast, LiCl could deposit within the pores of BPDG, as observed by the tight encapsulation of LiCl particles by the curved and interconnected graphene sheets. LiCl was well distributed and confined by these blocking pores with very fine nanoparticles (Fig. 2F). This result can be attributed to the superior mass diffusion kinetics in BPDG due to the larger accessible electrochemical surface area (181 F cm^{-2} for BPDG *versus* 108 F cm^{-2} for DG, Fig. 2G and Fig. S7, ESI†) and the required pore entrance, which facilitates electrolyte diffusion into these pores. Simultaneously, the pore could suppress the growth of LiCl particles without aggregation outside the pores by blocking the narrow pore entrance. As for the shrunk micropores in DG, the diffusion of electrolytes hinders access to the small micropores, and LiCl tends to deposit and agglomerate outside the pores.

After LiCl is deposited into the blocking pores during discharge, Cl_2 is produced in the pores upon subsequent charging. The confinement experiment of Cl_2 on BPDG also shows a significant advantage for containing Cl_2 due to the pore-entrance blocking effect. The porous graphene assembly (GA) fabricated by freeze-drying and subjected to the same heat treatment as BPDG/DG exhibits large mesopores and macropores (Fig. S8, ESI†); it was also used as a model to compare the ability for Cl_2 confinement with BPDG and DG. In this experiment, the mass usage (g) of these three carbons with different pore volumes per gram ($cm^3\ g^{-1}$) was adjusted to achieve an equal total pore volume (cm^3) for a fairer comparison. Cl_2 can react with a mixed solution (bright red under acidic conditions) containing potassium bromide (KBr) and methyl orange (Hln) to oxidize the potassium bromide to bromine, which further destroys the molecular structure of methyl orange and discolors the solution. We performed UV-vis spectroscopy on these carbons, and Fig. 2I and J shows the Cl_2 trapping effect of different carbon materials. According to the degree of discoloration, the absorbance was measured at ~505 nm for colorimetric determination. As a result, the absorption intensity of GA at ~505 nm showed a significantly smaller decrease compared with BPDG and DG, indicating a much inferior Cl_2 trapping ability for large meso- and macro-pores compared with the micropores and blocking pores. In addition, the tested absorbance intensity shows that BPDG traps more Cl_2 than DG, which can be ascribed to the narrow pore entrance blocking (Fig. 2I and J). The porous carbons (YP80F, PX15, and CMK-3) are also tested for Cl_2 containment, all showing inferior performance than BPDG (Fig. S9, ESI†). Raman spectra show that BPDG has a similar I_D/I_G ratio compared with DG (~1.9), which is significantly lower than that of control porous carbons (2.24–2.74) (Fig. S10, ESI†). Therefore, the higher Cl_2 trapping ability for BPDG with fewer carbon defects should mainly be ascribed to the blocking pore.

Facilitated LiCl deposition and Cl_2 trapping

The deposition and distribution of metal chloride are crucial in determining the chlorine conversion kinetics, and aggregated large LiCl particles tend to cause severe electrode passivation, while small LiCl particles favor fast chlorine conversion.[7] Thus, we further investigated the effect of BPDG and DG with the same total pore volume on the deposition behaviors of LiCl under electrochemical conditions. First, LiCl potentiation deposition experiments under 3.4 V were conducted to show the enhanced redox reactions enabled in BPDG (Fig. 3A and B). As a result, BPDG exhibits an earlier nucleation time than DG, confirming the superior nucleation kinetics of LiCl in the BPDG-based cathode. Moreover, the average total current densities of the DG and BPDG cathodes were calculated to be 0.14 mA cm^{-2} and 0.30 mA cm^{-2}, respectively, suggesting the improved deposition amount of LiCl in BPDG. The resultant LiCl deposition morphologies were also characterized by SEM, as shown in the inset images in Fig. 3A and B. In the BPDG-based cathode, the deposited LiCl particles are very fine, while the LiCl in DG is thick and agglomerated. After the initial discharge of the actual Li–Cl_2 battery, we used a confocal laser scanning microscope (CLSM) to observe the surface roughness of LiCl deposition. As shown in Fig. S11 (ESI†), the BPDG electrode shows a minor color change, whereas DG displays an apparent color evolution, illustrating a uniform LiCl deposition in BPDG and an aggregated LiCl-induced rough electrode surface in DG.

We also compared the electrochemical resistance of the battery using BPDG and DG in the cathodes. Electrochemical impedance spectroscopy (EIS) tests were conducted under various discharging/charging conditions, including first discharge to 700 mAh g^{-1}, discharge to 2 V, charging to 100 mAh g^{-1}, and charging to 700 mAh g^{-1} (Fig. 3C and Fig. S12, ESI†). The Nyquist plots shown in Fig. 3C consist of depressed semicircles and linear tails, and the semicircle diameter is positively correlated with the charge transfer resistance of R_{ct} for LiCl conversion. Specifically,

Published on 14 July 2025. Downloaded by Yunnan University on 8/3/2025 3:58:32 PM.

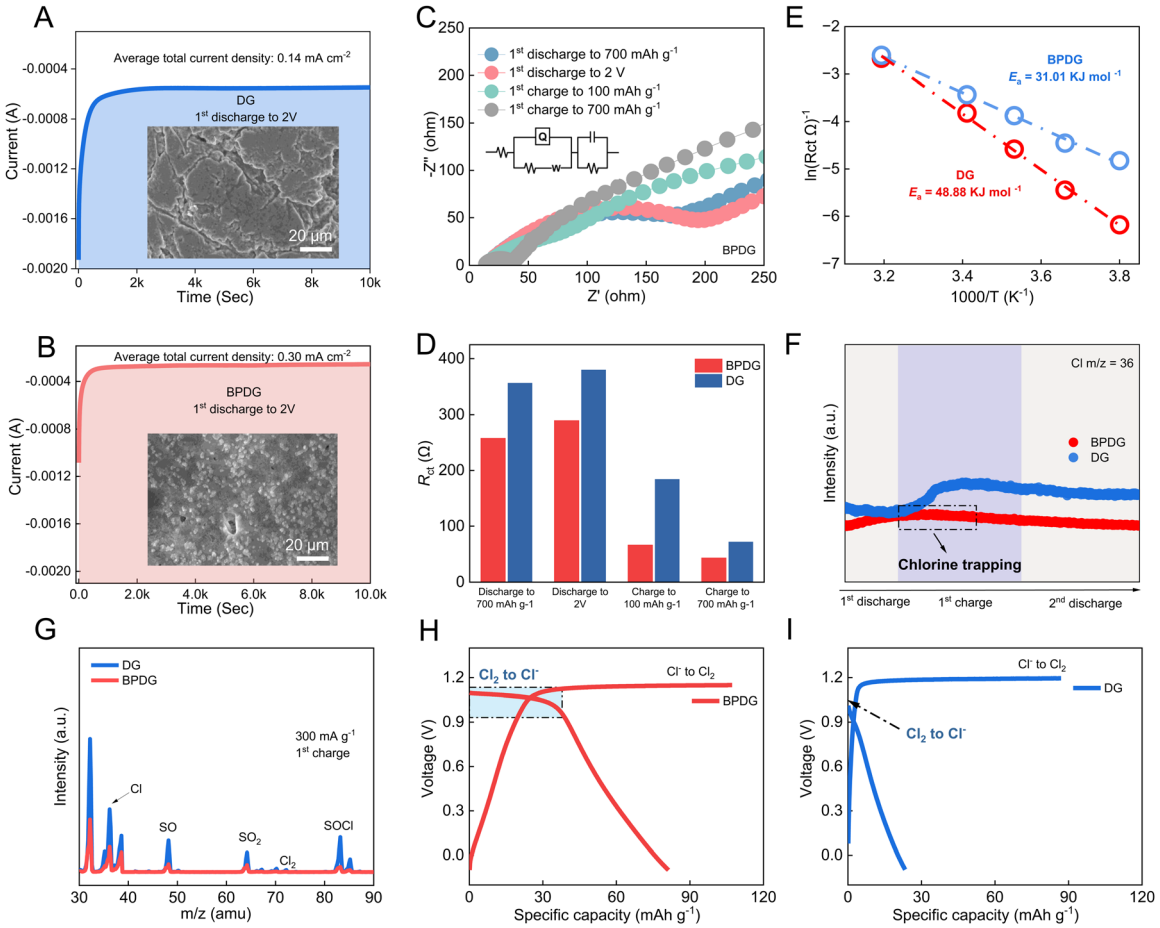

Fig. 3 LiCl deposition and Cl2 trapping characterizations under electrochemical conditions. (A) and (B) Potentiostatic discharge profiles tests for (A) BPDG and (B) DG at 3.4 V. The inset images show LiCl deposition on BPDG and DG. (C) EIS Nyquist plots of BPDG cells at different discharging/charging states. (D) R_{ct} comparisons between BPDG and DG cells. (E) Activation energy of interfacial Li^+ diffusion for BPDG and DG. (F) *In situ* DEMS of DG and BPDG cells, and (G) the Cl_2 signal intensity at the 4.1 V charging state. (H) and (I) Galvanostatic charge/discharge curves of (H) BPDG and (I) DG at 5 A g^{-1}.

when initially discharged to 700 mAh g^{-1}, the R_{ct} of BPDG is 257 Ω, much lower than that of DG with a R_{ct} of 356 Ω (Fig. 3D), confirming the superior interfacial charge transfer in BPDG. When the discharge proceeds to the final voltage of 2 V, the R_{ct} of BPDG (289 Ω) is still smaller than the R_{ct} (380 Ω) for DG, which may be attributed to the uniform LiCl deposition in BPDG upon the first discharging and lowering the electrochemical resistance of the Li–Cl_2 battery, as shown in Fig. 2F. Upon charging to 100 mAh g^{-1} and 700 mAh g^{-1}, both the R_{ct} values of BPDG and DG cells decrease compared with the discharging state due to the gradual electrochemical decomposition of LiCl into Cl_2. Meanwhile, the R_{ct} of BPDG is still smaller than that of DG, further proving that the facilitated uniform LiCl deposition and smaller LiCl particles favor its oxidation kinetics into Cl_2 upon charging. Furthermore, after LiCl deposition, the interfacial kinetics were also characterized by the temperature-dependent EIS from −10 °C to +40 °C (Fig. S13, ESI†), and the activation energy for Li^+ diffusion through the cathode interface was calculated based on the Arrhenius law. Consequently, a much lower activation energy (31.01 kJ mol^{-1}) during Li^+ diffusion through the LiCl interface was delivered for BPDG than that of DG (48.88 kJ mol^{-1}, Fig. 3E). The above results confirm that the large pore body and narrow pore entrance co-ordinately suppress the LiCl interfacial passivation in the cathode.

The Cl_2 evolution in Li–Cl_2 batteries is an important indicator of the rechargeability and stability of the electrodes and electrolytes.[3] The Cl_2 trapping in BPDG was investigated by *in situ* differential electrochemical mass spectrometry (DEMS). When LiCl was charged to form Cl_2, the Cl_2 trapping ability of BPDG and DG with the same total pore volume was explored during battery operation, and *in situ* DEMS was performed to monitor the chlorine formation inside the Li–Cl_2 battery during charge/discharge in real-time. Fig. 3F shows a much more obvious chlorine species increment for DG during the first charging than that of BPDG, which could be attributed to the chlorine species escaping from the aggregated LiCl on the surface of DG. In contrast, BPDG exhibits a relatively constant chlorine content during battery operations, demonstrating its excellent chlorine trapping ability by blocking the narrow pore entrance in BPDG. When specifically charging to a high voltage of 4.1 V, a higher chlorine fragmentation peak in mass over charge m/z = 36 amu and a stronger Cl_2 signal located in the

 This journal is © The Royal Society of Chemistry 2025

Published on 14 July 2025. Downloaded by Yunnan University on 8/3/2025 3:58:32 PM.

mass over charge m/z = 71 amu were observed in DG compared to BPDG (Fig. 3G), which indicates the enriched chlorine species in BPDG. Furthermore, to exclude the influence of the deposited LiCl on the Cl_2 confinement in porous carbon and the interference of other chlorine species, an electrochemical experiment was conducted in which we assembled a supercapacitor using BPDG or DG as the electrodes and the NaCl dissolved in water as the aqueous electrolyte to first produce a comparable amount of pure Cl_2 upon charging by controlling the oxidation time of Cl^- to Cl_2 and reduced these Cl_2 to Cl^- upon discharging. As a result, the BPDG electrode affords a significantly longer discharge platform with Cl_2 reduction to Cl^- (Fig. 3H). In sharp contrast, there is almost no Cl_2 in the DG electrode for reduction to Cl^-, resulting in a significantly lower reversible discharging capacity (Fig. 3I). The YP80F electrode was also tested in this experiment, showing very limited capacity from Cl_2 to Cl^- (Fig. S14, ESI†). This could be attributed to the produced Cl_2 being well contained in BPDG due to the narrow pore-entrance blocking effect, in contrast to the easy escape of Cl_2 from the open micropores. In addition, the observed flatter Li metal anode morphology in the BPDG cell compared with the DG cell also confirms the suppressed Cl_2 shuttling to the anode (Fig. S15, ESI†).

Chlorine conversion kinetic improvement

The improved chlorine conversion mechanism in BPDG was investigated using *in situ* Raman spectroscopy. *In situ* Raman spectroscopy of cathodes in different discharging/charging states was used to demonstrate the facilitated nanopore-confining conversion kinetics between LiCl and Cl_2 in BPDG. The charge/discharge curves within the voltage window from 2 to 4.3 V at 0.3 A g^{-1} are shown in Fig. 4A. The *in situ* Raman patterns of DG and BPDG are displayed in a two-dimensional (2D) color-filled contour plot (Fig. 4B and C). During the first discharging process, the characterized D ($\sim$1360 cm^{-1}) and G ($\sim$1580 cm^{-1}) bands of the DG in the Li–Cl_2 battery rapidly decreased with the decreasing potential applied, suggesting the production of LiCl and rapid coverage of the DG surface, and such peaks gradually disappeared at the fully discharged state due to the formation of thick LiCl. The D and G bands reappeared with LiCl oxidation into Cl_2 during the charging process, but the peak intensity was much weaker than the initial state (Fig. 4B). The evolutions of BPDG were also investigated by *in situ* Raman spectroscopy (Fig. 4C). During the initial discharging process, the stronger peak intensity of the D and G bands corresponds to the incomplete coverage by the deposited smaller LiCl particles. Moreover, the intensity of the D and G bands is completely restored to the initial state, confirming the reversible conversion from LiCl into Cl_2. More importantly, upon the second discharging process, the D and G bands of BPDG disappeared again due to a reversible transformation from Cl_2 to LiCl. These significant differences demonstrate that the blocking pores in BPDG achieve fast and reversible chlorine conversion.

The galvanostatic intermittent titration technique (GITT) was used to test the discharge equilibrium potential and IR drop (Fig. 4D). The Li–Cl_2 battery with BPDG exhibits a higher equilibrium potential (3.38 V) than the one with DG (3.27 V), which indicates improved energy efficiency. Correspondingly, the Li–Cl_2 battery with BPDG affords a 0.15 V IR drop, significantly smaller than that of the Li–Cl_2 battery with DG (0.25 V), which can be ascribed to the facilitated charge transfer and reaction kinetics in BPDG. The above-facilitated conversion between LiCl and Cl_2 was also evidenced by cyclic voltammetry (CV) tests. The CV analysis illustrated in Fig. 4E was performed using two electrodes in a coin cell, with BPDG or DG as the working electrode and Li metal as the counter electrode. Consequently, the reduction potential of Cl_2 (2.76 V) of the DG battery demonstrates a larger polarization and smaller peak current densities than that of the BPDG battery (the reduction potential is 3.04 V), indicating better chlorine conversion kinetics during reversible cycling. The superior chlorine conversion kinetics were also confirmed by the calculated lower formation energy for LiCl production ($* + Cl_2 + 2Li^+ + 2e^- \rightarrow *2LiCl$) using DFT calculations (Fig. 4F–H and Fig. S16–S18, ESI†). The nanopore confining Cl^- to LiCl has a lower formation energy of −8.82 eV (Fig. 4J and Fig. S19, ESI†) in BPDG, compared with the LiCl formation energy from Cl^- in the micropore model (−7.88 eV) and graphene model (−7.87 eV). In addition, the cycle life and polarization of Li–Cl_2 cells could both be optimized in BPDG with increased blocking pores by using more H_3PO_4 (Fig. 4I). The above result strongly confirms that the blocking pores in BPDG effectively facilitate chlorine conversion, and the induced confining chlorine conversion kinetics is superior to micropores and larger pores.

Electrochemical performance

Before evaluating the electrochemical performance improvement in BPDG, we provide a wider electrochemical performance comparison between BPDG, DG, GA, and the other typical porous carbons with higher SSA or larger pore volumes for use in Li–Cl_2 batteries, which includes the commonly used activated carbons with typical micropores of PX15 (2041 m^2 g^{-1}, 1.14 cm^3 g^{-1}) and YP80F (2100 m^2 g^{-1}, 0.94 cm^3 g^{-1}) and the typical mesopore carbon of CMK-3 (1022 m^2 g^{-1}, 1.0 cm^3 g^{-1}). We evaluated and compared the electrochemical performance of six porous carbons (BPDG, DG, GA, CMK-3, PX15, and YP80F) used in the Li–Cl_2 battery cathode (Fig. S20 and S21A, ESI†), which exhibited a high cut-off charging capacity of 2500 mAh g^{-1} and a high current density of 1 A g^{-1}. As a result, BPDG exhibits the highest reversible discharging capacity (2448 mAh g^{-1}) compared with DG (1460 mAh g^{-1}), GA (1534 mAh g^{-1}), CMK-3 (1649 mAh g^{-1}), PX15 (1836 mAh g^{-1}) and YP80F (1566 mAh g^{-1}), showing superior chlorine conversion reversibility (Fig. 5A). In addition, the BPDG cell also delivers a higher reduction potential (Fig. S21B, ESI†) and much lower polarization (0.34 V) than the other five porous carbons in a range of 0.46–0.78 V (Fig. 5A). In comparison with the other five carbons, the major difference of BPDG lies in its ability to block pores, achieving a more effective nanopore-confining chlorine conversion.

Subsequently, we focused on evaluating the application potential of BPDG for achieving high specific capacity, ultra-high rate capability, and long cycling stability. Fig. 5B shows that the discharge capacity of BPDG could afford 3863 mAh g^{-1}

Published on 14 July 2025. Downloaded by Yunnan University on 8/3/2025 3:58:32 PM.

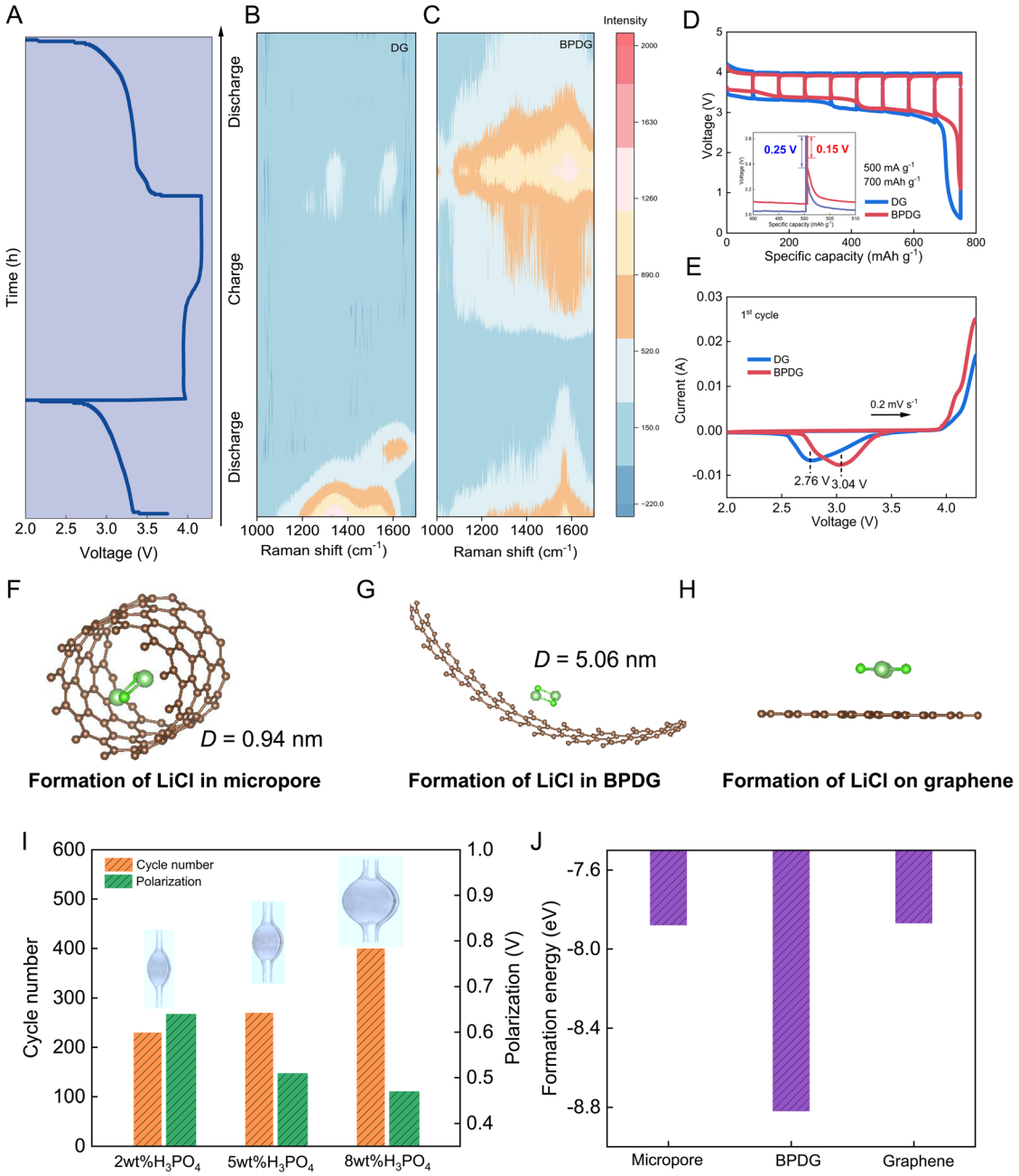

Fig. 4 Nanopore-confining chlorine conversion mechanism. (A) Galvanostatic charge/discharge curves of the Li–Cl_2 battery during the *in situ* Raman test. (B) and (C) *In situ* Raman spectroscopy of (B) DG and (C) BPDG at different discharging/charging states. (D) GITT curves of the BPDG battery and DG batteries. (E) CV curves of DG and BPDG cells at a scan rate of 0.2 mV s^{-1}. (F)–(H) LiCl formation energy for three cathode host models (micropores, blocking pores, and graphene). (I) Prolonged cycle life and decreased polarization with increasing blocking pores. (J) Calculated LiCl formation energy for the three cathode host models (micropores, blocking pores, and graphene).

when increasing the cut-off capacity to approach 4000 mAh g^{-1}. Comprehensively, the blocking pore designs significantly improve the reversible conversion efficiency of chlorine species, achieving a high reversibility of up to 98% at a cut-off capacity of 2500 mAh g^{-1}, which is much higher than that of other carbon materials (60–70%, Fig. 5C). Even at a cut-off capacity of up to 4000 mAh g^{-1}, the BPDG cell could also deliver a high reversibility of 96.6% (Fig. 5C). In addition, the LiCl utilization ratio could be calculated by the cycling capacity of LiCl/Cl_2 conversion divided by the initial discharging capacity of $SOCl_2$ reduction into LiCl.[17] In this work, the initial discharging capacity is 5208 mAh g^{-1} (Fig. S22, ESI†), and the maximal cycling capacity is 3863 mAh g^{-1}. Thus, the LiCl utilization ratio is calculated to be ~74% (3863/5208 mAh g^{-1}), illustrative of the high chlorine utilization of the Li–Cl_2 cell. The gravimetric capacity is one of the highest values reported in Li–Cl_2 batteries

 This journal is © The Royal Society of Chemistry 2025

Published on 14 July 2025. Downloaded by Yunnan University on 8/3/2025 3:58:32 PM.

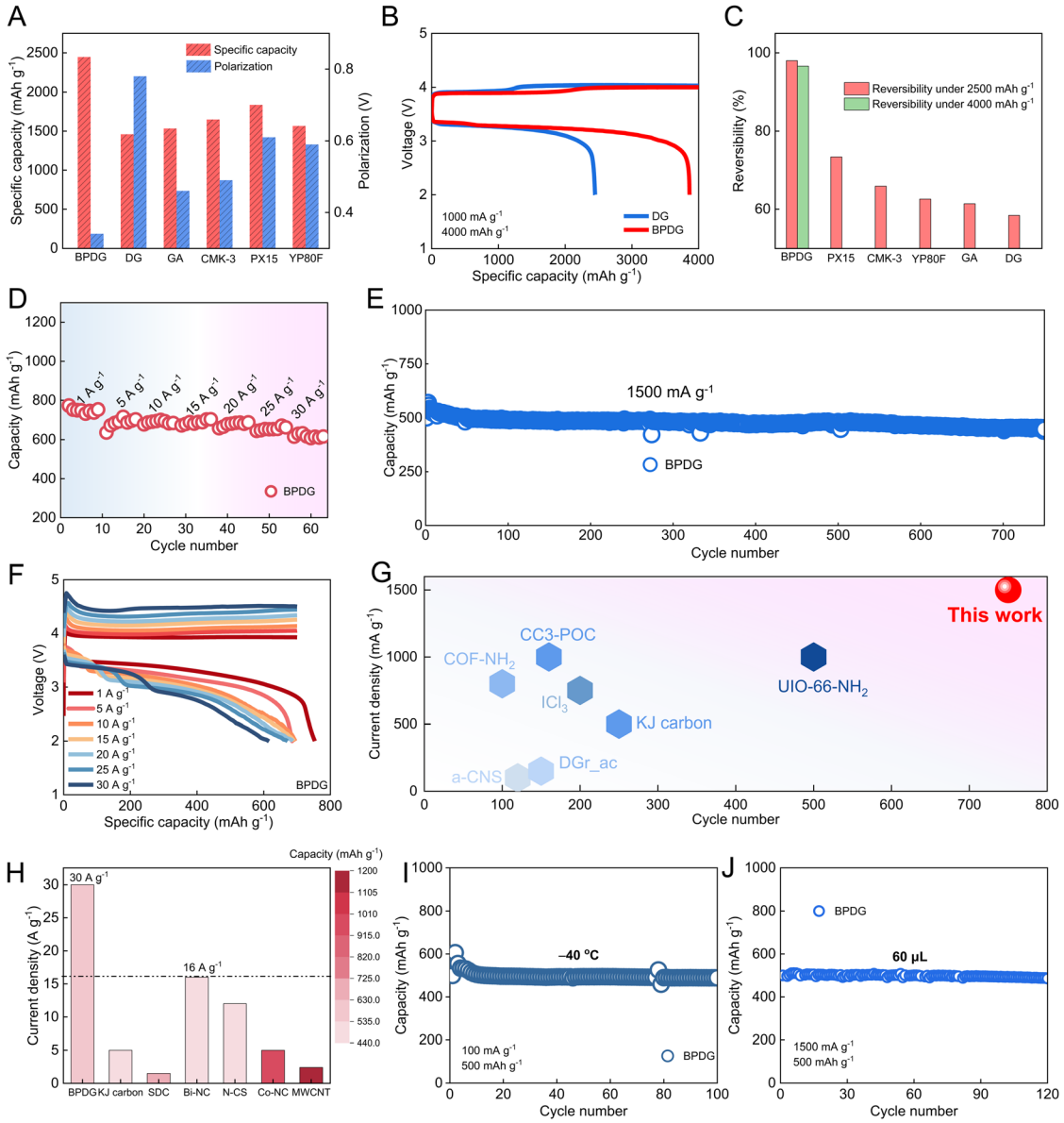

Fig. 5 Electrochemical performance characterizations. (A) Reversible discharging capacity and polarization comparisons among BPDG, DG, GA, CMK-3, PX15, and YP80F with a cut-off capacity of 2500 mAh g^{-1} at a current density of 1.0 A g^{-1}. (B) Charge–discharge curve of the BPDG battery with a cut-off capacity of 4000 mAh g^{-1} at a current density of 1.0 A g^{-1}. (C) Comparison of charge–discharge reversibility under different cut-off capacities of 2500 mAh g^{-1} and 4000 mAh g^{-1} for the six carbons. (D) Rate performance of Li–Cl_2 battery at current densities from 1 to 30 A g^{-1}. (E) Cycling performance of the BPDG battery with a charge capacity of 500 mAh g^{-1} at a current density of 1.5 A g^{-1}. (F) Charge–discharge curves of the BPDG battery at current densities from 1 to 30 A g^{-1}. (G) Cycle life comparisons between BPDG and other reported Li–Cl_2 batteries. (H) Rate performance comparison between the BPDG Li–Cl_2 cell and other high-rate-capability Li/Na–Cl_2 batteries. (I) Cycling performance at a low temperature of −40 °C. (J) Cycling performance under lean electrolyte of 60 µL.

(Table S1, ESI†), which represents a blocking pore that achieves higher pore filling of the active chlorine species and superior chlorine conversion efficiency, in sharp contrast to open pores enduring Cl_2 spillage or LiCl agglomeration.

Fig. 5D shows the rate performance of Li–Cl_2 batteries with BPDG at different current densities. Specifically, the Li–Cl_2 batteries with BPDG show a specific charging capacity of 700 mAh g^{-1} at an initial current density of 1 A g^{-1}. Impressively, at an ultrahigh current density of 30 A g^{-1}, the BPDG cell delivers a high specific discharge capacity of 616 mAh g^{-1}. Fig. 5F shows the discharging–charging curve changes with the increased current density from 1 A g^{-1} to 30 A g^{-1}, and the BPDG cell shows very slowly increasing polarizations with the increasing current densities (Fig. S23A, ESI†). Impressively, this charging current density of 30 A g^{-1} is six times higher than the previously reported highest value for Li–Cl_2 batteries (5 A g^{-1}, ~500 mAh g^{-1}, Fig. 5H). This current density is even almost two times higher than the previously reported record value, including Na–Cl_2 batteries (16 A g^{-1}, Table S1, ESI†),[16] and this remarkable rate performance similarly confirms the

Published on 14 July 2025. Downloaded by Yunnan University on 8/3/2025 3:58:32 PM.

advantage of applying a continuous interconnected carbon network in the Li–Cl_2 battery cathode for boosting the charge transport kinetics[16] and more importantly, highlights the blocking pores to facilitate chlorine conversion kinetics significantly. Furthermore, a high current density of 1.5 A g^{-1} was used to charge the BPDG battery and evaluate its cycling performance at a specific capacity of 500 mAh g^{-1}. The BPDG battery exhibited long cycle stability of over 750 cycles at a high current density of 1.5 A g^{-1} (Fig. 5E), which is significantly superior to the cycle life reported in the literature (all of which not exceeding 500 cycles at lower current densities, Fig. 5G and Table S1, ESI†). Notably, the polarization of the BPDG battery has a minor increase, with the cycle proceeding even over 500 cycles. At the 5th, 100th, 200th, 300th, and 500th cycle, the polarizations are 0.65 V, 0.54 V, 0.52 V, 0.60 V, and 0.77 V, respectively (Fig. S23B, ESI†). The cycling performance test under a higher specific capacity of 2000 mAh g^{-1} also shows excellent stability (Fig. S24, ESI†). The energy density calculated on the mass of cathode materials (LiCl and carbon) is 1771 Wh kg^{-1}.

The electrochemical performance of Li–Cl_2 batteries was then tested under extreme conditions to demonstrate the practicability. Specifically, the BPDG battery can afford a very stable 100-cycle life under a low temperature of −40 °C and a specific capacity of 484 mAh g^{-1} after cycling (Fig. 5I). The discharge–charge curves along the cycling show excellent chlorine conversion reversibility (Fig. S25, ESI†). The electrochemical performance tests on the battery at various low temperatures (*e.g.*, cycling performance ranging from 0 °C to −40 °C) were conducted to further substantiate the excellent low-temperature tolerance. As a result, the BPDG cathode exhibits a much superior capacity retention and lower polarization from 0 °C to −40 °C compared with the DG cathode in Li–Cl_2 batteries (Fig. S26, ESI†). The XRD spectra show the LiCl production after the first discharge, and the SEM image reveals that the BDPG particle has a porous carbon framework, without large LiCl particle formation. The above results demonstrate the good LiCl deposition kinetics enabled by the blocking pore even at a low temperature of −40 °C (Fig. S27, ESI†). The HRTEM and N_2 adsorption–desorption isotherms of the low temperature-treated BPDG show an obvious blocking pore configuration with a narrow pore neck and large pore body (Fig. S28, ESI†), confirming its structural stability under extreme conditions.

For battery conditions with less electrolyte, the BPDG battery can operate stably over 120 cycles using a lean electrolyte of 60 μL (Fig. 5J, the previously reported Li–Cl_2 battery usually uses at least 100–150 μL of the electrolyte), which also presents good chlorine redox reversibility (Fig. S29A, ESI†). Notably, this is the best cycling performance, given the low electrolyte addition and high specific capacity (Table S1, ESI†). Even with the addition of 40 μL of electrolyte, the BPDG battery could work normally with a relatively low polarization (0.5 V) and excellent reversibility under a specific capacity of 525 mAh g^{-1} (Fig. S29B, ESI†). To further demonstrate the superiority of our BPDG cathode host for practical applications, pouch-cell batteries were assembled with a BPDG cathode host. The pouch Li–Cl_2 battery could deliver a relatively stable 50-cycle life at a current density of 0.3 A g^{-1} and charging capacity of 500 mAh g^{-1} (Fig. S30, ESI†).

The SCl_2, S_2Cl_2, and SO_2Cl_2 species were produced by the oxidation of $SOCl_2$ and by the reaction between Cl_2 and the S/SO_2 dissolved in the electrolyte.[37] However, the conversion of Cl_2 to these S–Cl species only occurred under high charging capacity, high charging voltage (Fig. 5B), high charging current densities (Fig. 5F) or low temperatures (Fig. S25, ESI†). Nevertheless, (1) the conversion between Cl_2 and LiCl is still the main battery reaction, and (2) these products of SCl_2, S_2Cl_2, and SO_2Cl_2 are also reversible in the subsequent discharging procedure, which occurred at the beginning (SCl_2 and S_2Cl_2) or the end (SO_2Cl_2) of the main Cl_2 discharge plateau.[38] As an important electrochemical proof, the Cl_2 reduction in discharging occupies the main part, which is accompanied by the reversible reduction of SCl_2, S_2Cl_2, and SO_2Cl_2 in the typical charge–discharge curve of Li–Cl_2 battery using BPDG under a high specific capacity of 2500 mAh g^{-1} (Fig. S21B, ESI†). Fig. S31 (ESI†) shows the EDS mapping of the charged BPDG particle after rinsing, where the overlapped Cl, S, and O signals may be ascribed to other charging products, including SCl_2, S_2Cl_2, and SO_2Cl_2, trapped inside blocking porous carbons. Furthermore, Fig. S32(ESI†) shows the much lower polarizations for the electrochemical conversion of S–Cl products in blocking pores compared with other porous carbons (all higher than 0.35 V). Fig. S33 (ESI†) shows the specific interfacial resistance under different charging–discharging states of Cl_2 and S–Cl species. It can be seen that BDPG exhibits lower interfacial resistance not only for Cl_2 conversion but also for the SCl_2, S_2Cl_2, and SO_2Cl_2 conversions, indicating that the blocking pore can facilitate the S–Cl species transformation through pore confinement. Therefore, the formed SCl_2, S_2Cl_2, and SO_2Cl_2 products are electrochemically reversible and tend to be trapped and facilitated in conversion by the confinement of the blocking pore.

Conclusions

To improve the rechargeability of Li–Cl_2 batteries, we present a blocking pore design towards a high pore utilization ratio and nanopore confining chlorine conversion for Li–Cl_2 battery cathodes by integrating the chlorine confinement ability, which is demonstrated by pores with large pore body (~5–16 nm) and narrow pore entrance (~3.8 nm). This kind of pore features a narrow pore-entrance blocking effect. Specifically, in discharging, the LiCl could uniformly deposit into the large pore body, and its growth could be confined by the pore entrance to form uniform fine nanoparticles. Also, the tightened, narrow pore entrance could suppress the produced Cl_2 spillage and shuttle during the subsequent reversible charging process. The blocking-pore confinements of LiCl and Cl_2 are comprehensively characterized by HRTEM, Cl_2 adsorption, *in situ* DEMS, and Raman tests. As a result, the high utilization of Cl_2 and LiCl in blocking pores enables a high gravimetric capacity of 3863 mAh g^{-1} for Li–Cl_2

 This journal is © The Royal Society of Chemistry 2025

Published on 14 July 2025. Downloaded by Yunnan University on 8/3/2025 3:58:32 PM.

batteries. Moreover, the enhanced conversion kinetics achieved by the effective nanopore confinement of chlorine conversion between Cl_2 and LiCl delivers a super-long cycle life (750 cycles) and remarkable rate capability (616 mAh g^{-1} at 30 A g^{-1}). This work presents an important pore confinement mode to address both the low pore utilization ratio and chlorine conversion efficiency in metal–chlorine batteries fundamentally.

Methods

Preparation of DG and BPDG

A graphene oxide (GO) suspension (80 mL, 2 mg mL^{-1}) was prepared by adding 16 mL of a graphite oxide solution (10 mg mL^{-1}) to 64 mL of water and sonicated for 2 h. Typically, the homogeneous GO suspension was placed in a Teflon-lined autoclave and treated by a hydrothermal process in a muffle furnace (180 °C) for 6 h, producing a cylindrical graphene hydrogel with a diameter of ≈2.4 cm and a height of ≈2.5 cm. This hydrogel was treated with evaporation-induced capillary drying at 70 °C for 48 h, followed by thermal heat (600 °C) for 1 h under argon (Ar)-flowing conditions to obtain a dense, continuous graphene network with a main microporous structure (DG). For the BPDG preparation, the graphene hydrogel was fully soaked in a 20 mL H_3PO_4 aqueous solution (8 wt% concentration) for 12 h of static adsorption and then subjected to vacuum drying. Subsequently, the mixture was subjected to evaporation-induced capillary drying at 70 °C for 48 h, followed by thermal heating at 600 °C for 1 h under Ar-flowing conditions to obtain a dense, continuous graphene network with a blocking-pore structure. After cooling to room temperature, the sample was repeatedly washed with 1 M hydrochloric acid (HCl) solution and water, followed by drying overnight to yield the final product BPDG (with a typical diameter of ≈0.5 cm and height of ≈0.6 cm).

Preparation of $SOCl_2$-based electrolyte

The Li–Cl_2 battery electrolyte was prepared in an Ar-filled glovebox with water and oxygen levels not exceeding 0.01 ppm. $AlCl_3$ (99.0%, Alfa), $SOCl_2$ (99%, Aladdin), LiFSI (DoDoChem), and LiTFSI (DoDoChem) were used without any further purification. Firstly, 4 M of $AlCl_3$ powder was added to 1 mL of $SOCl_2$ solution and stirred until the $AlCl_3$ was fully dissolved. Subsequently, specific amounts of LiFSI and LiTFSI powder (2 wt% of the total weight of $AlCl_3$ and $SOCl_2$) were added to the above $SOCl_2$ solution and stirred until complete dissolution. In this $SOCl_2$-based electrolyte, $AlCl_3$ will react with LiCl that is generated upon $SOCl_2$ passivating the Li metal anode surface and upon the first discharging process to convert into $Li[AlCl_4]$ as an ion conductor, while the LiTFSI and LiFSI additives will regulate the composition of the SEI of the anode.

Preparation of cathodes

80% by weight of either DG or BPDG powder, 10% by weight of carbon black, and 10% by weight of polyvinylidene difluoride (PVDF) were mixed in 100% *N*-methylpyrrolidone (NMP). The mixture was then mixed for 30 minutes. The obtained slurry was deposited onto a stainless-steel sheet collector with a diameter of 15.5 mm and then dried in an oven at 80 °C until all the NMP had evaporated. The mass loading of this carbon support for the electrochemical performance test is ∼2.0 mg cm^{-2}.

Preparation of Li–Cl_2 batteries

All batteries were assembled within the Ar-filled glovebox. For the Li–Cl_2 batteries, DG or BPDG cathode with stainless steel as the current collectors, glass fiber filter (GF/D, Whatman) with a diameter of 19 mm, Li anode at the center of a CR2032 coin battery, with a certain amount of the above $SOCl_2$-based electrolyte (100 μL) added onto the separators. The detailed Li–Cl_2 battery assemblies are shown in Fig. S20 (ESI†). Finally, the CR2032 coin battery was kept on the top, and the entire battery was sealed using a pressure-controlled crimper. The lean electrolyte conditions involve decreasing the volume of electrolytes from 60 μL to 40 μL, respectively.

Preparation of Li–Cl_2 pouch batteries

The pouch Li–Cl_2 cell consists of a BPDG cathode, a glass fiber separator (GF/D, Whatman), a Li metal anode, and a $SOCl_2$-based electrolyte. First, a flexible battery shell (Al-plastic composite film) was prepared. Then, to prepare the cathode, we used a blade to cut the BPDG film into about 4 cm (length) × 6 cm (width). After the cathode was welded, 400 μL of electrolyte was injected and placed in a shell to seal and ensure good sealing. The assembled pouch cell size is 5 cm (length) × 8 cm (width).

Materials characterizations

The morphology of samples was captured by TEM (Thermo Scientific Talos F200X) and SEM (Hitachi Regulus 8230). The XRD patterns were characterized between 10°–90° with a scan rate of 5° min^{-1} by a Bruker-AXS D8 Advance. N_2 adsorption–desorption isotherms (77 K) were measured by a BELSORP MAX G (Microtrac MRB). Samples of ≈100 mg were heated at 200 °C under vacuum to remove all adsorbed species. Specific surface area and pore size distribution were determined using the Brunauer–Emmett–Teller (BET) and non-local density functional theory (NLDFT) methods. The depositional morphology of LiCl was captured by a confocal laser scanning microscope (CLSM).

Adsorption test of Cl_2

Cl_2 was prepared by slowly adding concentrated hydrochloric acid dropwise to potassium permanganate ($KMnO_4$), and pure chlorine gas was collected in a collecting cylinder. Porous carbons were placed in a chlorine-filled cylinder for 5 h for static adsorption. 0.1000 g of methyl orange was weighed and dissolved in about 100 mL of hot water (50 °C) and cooled; 20 mL of 95% ethanol was added and the solution was transferred quantitatively with water into a 1000 mL volumetric flask, and diluted to scale. Then, 50 ml of this solution is added to a 500 ml volumetric flask, followed by 1 g of potassium

Published on 14 July 2025. Downloaded by Yunnan University on 8/3/2025 3:58:32 PM.

bromide and water. 400 mL of this solution was mixed with 100 mL of sulphuric acid (2.57 mol L^{-1}) to prepare an absorbent solution. After a long adsorption of Cl_2 and a subsequent 12 h placement in the Ar atmosphere, these carbons were immersed in the absorbent solution. Ultraviolet-visible (UV-vis) spectroscopy was performed on the absorbent solution using a UV-3600 spectrophotometer in the wavelength range of 350–650 nm.

Electrochemical performance measurements

Unless otherwise stated, all electrochemical measurements were conducted at 25 °C in a Land CT3002A thermostatic test chamber. Low-temperature measurements were carried out in freezers (DW-40L348J). The charge–discharge performance of the batteries was obtained using the Land and Neware battery testing system. The CV was acquired at the Gamry electrochemical work station with a potential of 2–4.2 V. GITT was tested by executing multiple 20-minute (pulse time, τ) pulsed currents (0.05 A g^{-1}), followed by 120 minutes of relaxation intervals across the entire range of relevant voltages. The assembled button cell batteries are tested for constant potential deposition curves after 3 turns of charge/discharge testing on the LAND test system. Constant potential deposition was carried out at a potential of 3.4 V to investigate the deposition of LiCl on the surfaces of different materials (test time 10 000 s). The deposition curves were integrated to calculate the current density. *In situ* DEMS was conducted on AS 100Li (Iridium filament, 5×10^{-4} A per mbar) with a mass range of 1–100. EIS was performed using the potentiostatic mode at the open-circuit voltage on a Gamry electrochemical workstation. A sinusoidal voltage with an amplitude of 10 mV and a frequency range from 0.1 Hz to 10 kHz was applied. A high and low-temperature alternating test chamber (DW-40L348J) was used in conjunction with the Gamry electrochemical workstation to measure the impedance at temperatures ranging from −10 °C to 0 °C, 10 °C, 20 °C, and 40 °C, respectively. The interval time between each temperature was 30 min. The equivalent circuit models were established, and parameters involved in the electrochemical processes, such as the contact resistance and the charge transfer resistance, were fitted. The values of activation energy for the charge transfer process were further calculated according to the classic Arrhenius equation as follows:

$$R_{ct} = k e^{-\frac{E}{RT}}.$$

R_{ct} refers to the charge transfer resistance, k is the pre-exponential factor, R is the molar gas constant (8.314 J mol^{-1} K^{-1}), T is the applied temperature in the EIS measurements, and E is the activation energy.

Note:

Gravimetric capacity (mAh g^{-1}) = (capacity in mAh)/(carbon mass in g)

Energy density calculation based on the cathode materials (LiCl and carbon) (Wh kg^{-1}) = (capacity in mAh × voltage in V)/(LiCl mass in mg + carbon mass in mg)

The calculation of ECSA

The electrodes were prepared by mixing DG or BPDG, PVDF, and carbon black at a weight ratio of 8 : 1 : 1 in NMP solvent. The mixture was then mixed for 30 minutes. The obtained slurry was deposited onto a stainless-steel sheet collector with a diameter of 15.5 mm and then dried in an oven at 80 °C until all the NMP had evaporated. The two identical electrodes were assembled into a standard CR2032 coin cell with a GF/D Celgard membrane serving as the separator, and 100 μL of the as-prepared $SOCl_2$ solution was used as the electrolyte. CV measurements of the symmetric batteries were measured between 0.4–0.5 V at different scan rates from 2 mV s^{-1} to 10 mV s^{-1}. In a series of curves with different sweep rates, the current density and sweep rate at a certain potential are selected for plotting to obtain a straight line, and the slope of the straight line is the double layer capacitance C_{dl}. The capacitance and the active surface area are proportional to the specific surface area.

Cl_2/Cl^- conversion experiment

We assembled a supercapacitor using BPDG, DG, or YP80F as the electrodes and NaCl dissolved in water as the aqueous electrolyte. The working electrode was made by mixing the active material, carbon black, and polyvinylidene fluoride (PVDF) in 100% *N* methyl pyrrolidone (NMP) at a weight ratio of 8 : 1 : 1. The current constant-current charge/discharge curves were obtained in a three-electrode cell with an activated carbon counter electrode and an Ag/AgCl reference electrode (0.197 V relative to NHE). The galvanostatic current charge/discharge curves were obtained by a CHI760E electrochemical workstation at a current density of 5 A g^{-1}.

In situ Raman spectroscopy

The electrode for *in situ* Raman spectroscopy was prepared using the following steps. The carbon was mixed with carbon black and PVDF in a weight ratio of 8 : 1 : 1 using NMP as the solvent. The above slurry was rolled into a film and dried at 80 °C. The electrode for *in situ* Raman spectroscopy was obtained by compressing the prepared film on the stencil mesh current collector. *In situ* Raman spectroscopy was performed with the HORIBA HR Evolution with a 532 nm wavelength. The charge/discharge measurements were performed on Landt battery test systems during *in situ* Raman tests.

DFT calculation

All periodic DFT calculations were performed using the Vienna *Ab Initio* Simulation Package (VASP), which employs projector augmented wave (PAW) pseudopotentials to model the core-valence interactions, along with the Perdew–Burke–Ernzerhof (PBE) exchange–correlation functional within the framework of the generalized gradient approximation (GGA). The plane-wave cut-off energy was set to 500 eV. For the modeling, a graphene model with a 4 × 4 × 1 cell expansion of the protocell was used to obtain a 32-atom graphene model for relaxation. The other two porous carbons were modeled as carbon structures with

 This journal is © The Royal Society of Chemistry 2025

Published on 14 July 2025. Downloaded by Yunnan University on 8/3/2025 3:58:32 PM.

inner pore diameters of 0.94 nm and 5.06 nm, respectively, and the number of atoms relaxed was 96 and 296, respectively. The distances of Cl_2 after relaxation to graphene, CNT of d = 0.94 nm and CNT of d = 5.06 nm are 3.81 Å, 4.01 Å and 3.96 Å, respectively, and the distances of 2LiCl to graphene, CNT of d = 0.94 nm and CNT of d = 5.06 nm are 3.72 Å, 2.66 Å and 3.92 Å, respectively. The molecules are influenced by the substrate due to electrostatic interactions and do not exhibit chemisorption states (no bonding interactions with the defect-free carbon material). The Brillouin zone in reciprocal space was sampled using a Γ-centred Monkhorst–Pack grid, with $9 \times 9 \times 1$ k-points for geometry optimization and electronic structure calculations (graphene) with $4 \times 4 \times 6$ k-points for geometry optimization and electronic structure calculations (9.37A-carbon nanotube model) with $1 \times 1 \times 10$ k-points for geometry optimization and electronic structure calculations (50.6A-carbon nanotube model). An energy smearing of 0.05 eV was applied to accelerate convergence using the first-order Methfessel–Paxton scheme. Geometry optimization was conducted using the conjugate gradient algorithm, with a convergence criterion of 10^{-8} eV for the total energy per atom and a force convergence threshold of 0.02 eV $Å^{-1}$ based on the Hermann–Feynman forces.

The relative free energy for the discharging process is calculated using the formula:

$$G = E + \mathrm{ZPE} - TS$$

The relative free energy for the discharging process from Li^+ and Cl_2 to LiCl on the substrate is calculated based on the reaction sequence:

$$Cl_2 + 2Li^+ + * \rightarrow *2LiCl$$

The reaction energies corresponding to several steps are calculated using the formula:

$$2E_{\mathrm{LiCl}^*} - (2E_{\mathrm{LiCl}} + E_{\mathrm{sub}})$$

$$2E_{\mathrm{Cl}^*} - (E_{\mathrm{Cl}_2} + E_{\mathrm{sub}})$$

Author contributions

L. J. Z., Q. H. Y., and D. B. K. conceived and supervised the research. J. W. H. designed the experiments. J. W. H. and X. R. W. performed the main research experiments. G. Z. M., H. W., Y. M. S., Z. H. L., L. Z., C. Y. M., Q. H. L. and W. T. F. helped with material characterizations. W. L. contributed to discussions on experimental details and the framework of the work. J. W. H. wrote the manuscript under the guidance of D. B. K. Q. H. Y. and L. J. Z.

Conflicts of interest

There are no conflicts to declare.

Data availability

The data supporting this article have been included as part of the ESI.†

Acknowledgements

This work was supported by the National Natural Science Foundation of China (52473285 and 92372204), the Shenzhen Science and Technology Program (KJZD20240903100900002), the Taishan Scholar Project of Shandong Province (tsqn202211086, ts202208832, and tsqnz20221118), the Natural Science Foundation of Shandong Province (ZR2024QE130), and the Fundamental Research Funds for the Central Universities (23CX06055A).

References

1 G. Zhu, X. Tian, H.-C. Tai, Y.-Y. Li, J. Li, H. Sun, P. Liang, M. Angell, C.-L. Huang and C.-S. Ku, *et al.*, *Nature*, 2021, **596**, 525–530.
2 P. Liang, G. Z. Zhu, C. L. Huang, Y. Y. Li, H. Sun, B. Yuan, S. C. Wu, J. C. Li, F. F. Wang and B. J. Hwang, *et al.*, *Adv. Mater.*, 2024, **36**, 2307192.
3 Y. Xu, S. X. Zhang, M. M. Wang, Y. H. Meng, Z. H. Xie, L. D. Sun, C. Huang and W. Chen, *J. Am. Chem. Soc.*, 2023, **145**, 27877–27885.
4 B. Yuan, Q. C. Xu, X. J. Zhao, S. T. Geng, S. S. Tang, C. X. Zhang and H. Sun, *Adv. Energy Mater.*, 2024, **14**, 2303127.
5 B. Yuan, L. Wu, S. T. Geng, Q. C. Xu, X. J. Zhao, Y. Wang, M. Liao, L. Ye, Z. T. Qu and X. Zhang, *et al.*, *Angew. Chem., Int. Ed.*, 2023, **62**, 2306789.
6 Z. H. Xie, L. D. Sun, M. Sajid, Y. C. Feng, Z. S. Lv and W. Chen, *Chem. Soc. Rev.*, 2024, **53**, 8424–8456.
7 W. T. Feng, X. R. Wei, J. H. Yang, C. Y. Ma, Y. M. Sun, J. W. Han, D. B. Kong and L. Zhi, *J. Nat. Commun.*, 2024, **15**, 6904.
8 G. D. Chen, W. D. Li, X. F. Du, C. Wang, X. L. Qu, X. Y. Gao, S. M. Dong, G. L. Cui and L. Q. Chen, *J. Am. Chem. Soc.*, 2023, **145**, 22158–22167.
9 P. Liang, G. Zhu, C. L. Huang, Y. Y. Li, H. Sun, B. Yuan, S. C. Wu, J. Li, F. Wang and B. J. Hwang, *et al.*, *Adv. Mater.*, 2024, **36**, e2307192.
10 P. Li, S. Yang, J. X. Zhu, S. N. Wang, Y. Hou, H. L. Cui, Z. Chen, R. Zhang, Z. X. Wu and Y. Q. Wang, *et al.*, *Matter-Us*, 2024, **7**, 1867–1878.
11 Q. Guo, K.-I. Kim, S. Li, A. M. Scida, P. Yu, S. K. Sandstrom, L. Zhang, S. Sun, H. Jiang and Q. Ni, *et al.*, *ACS Energy Lett.*, 2021, **6**, 459–467.
12 G. Chen, X. Liu, H. Hou, X. Gao, L. Hu, S. Dong and G. Cui, *Sci. Bull.*, 2024, 140–143.
13 G. Zhu, P. Liang, C.-L. Huang, C.-C. Huang, Y.-Y. Li, S.-C. Wu, J. Li, F. Wang, X. Tian and W.-H. Huang, *et al.*, *J. Am. Chem. Soc.*, 2022, **144**, 22505–22513.
14 S. L. Chen, L. Wu, Y. Liu, P. Zhou, Q. Y. An and L. Q. Mai, *J. Energy Chem.*, 2024, **88**, 154–168.
15 W. T. Feng, J. H. Yang, X. R. Wei, C. Y. Ma, J. W. Han, G. Z. Ma, H. Wang, D. B. Kong and L. J. Zhi, *Angew. Chem., Int. Ed.*, 2025, e202503752, DOI: **10.1002/anie.202503752**.

Published on 14 July 2025. Downloaded by Yunnan University on 8/3/2025 3:58:32 PM.

16 L. X. Xiang, Q. C. Xu, H. Zhang, S. T. Geng, R. Cui, T. Y. Xiao, P. N. Chen, L. Wu, W. Yu and H. S. Peng, *et al.*, *Angew. Chem. Int. Ed.*, 2023, **62**, 2312001.
17 Y. Xu, M. M. Wang, M. Sajid, Y. H. Meng, Z. H. Xie, L. D. Sun, J. Jin, W. Chen and S. X. Zhang, *Angew. Chem., Int. Ed.*, 2024, **63**, e202315931.
18 Y. Xu, L. Jiao, J. L. Ma, P. Zhang, Y. F. Tang, L. M. Liu, Y. Liu, H. H. Ding, J. F. Sun and M. M. Wang, *et al.*, *Joule*, 2023, **7**, 515–528.
19 G. Z. Zhu, P. Liang, C. L. Huang, S. C. Wu, C. C. Huang, Y. Y. Li, S. K. Jiang, W. H. Huang, J. C. Li and F. F. Wang, *et al.*, *Proc. Natl. Acad. Sci. U. S. A.*, 2023, **120**, 2310903120.
20 X. T. Fan, K. Huang, L. Chen, H. P. You, M. L. Yao, H. Jiang, L. Zhang, C. Lian, X. W. Gao and C. Z. Li, *Angew. Chem., Int. Ed.*, 2023, **62**, 2215342.
21 C. Y. Ma, W. T. Feng, D. B. Kong, X. R. Wei, X. L. Gong, J. H. Yang, J. W. Han and L. J. Zhi, *Small*, 2024, **20**, 2310978.
22 X. R. Wei, D. B. Kong, W. T. Feng, F. L. Cao, C. Y. Ma, J. H. Yang, J. W. Han, L. Wang, G. Z. Ma and H. Wang, *et al.*, *Adv. Energy Mater.*, 2025, 202501333, DOI: **10.1002/aenm.202501333**.
23 Y. S. Lin, *Curr. Opin. Chem. Eng.*, 2015, **8**, 21–28.
24 H. Li, Y. Tao, C. Zhang, D. H. Liu, J. Y. Luo, W. C. Fan, Y. Xu, Y. Z. Li, C. H. You and Z. Z. Pan, *et al.*, *Adv. Energy Mater.*, 2018, **8**, 1703438.
25 W. Lv, C. Zhang, Z. J. Li and Q. H. Yang, *J. Phys. Chem. Lett.*, 2015, **6**, 658–668.
26 Y. Tao, X. Y. Xie, W. Lv, D. M. Tang, D. B. Kong, Z. H. Huang, H. Nishihara, T. Ishii, B. H. Li and D. Golberg, *et al.*, *Sci. Rep.*, 2013, **3**, 2975.
27 C. S. Qi, C. Luo, Y. Tao, W. Lv, C. Zhang, Y. Q. Deng, H. Li, J. W. Han, G. W. Ling and Q. H. Yang, *Sci. China-Mater.*, 2020, **63**, 1870–1877.
28 C. Zhang, W. Lv, Y. Tao and Q. H. Yang, *Energy Environ. Sci.*, 2015, **8**, 1390–1403.
29 B. S. Girgis and A.-N. A. El-Hendawy, *Microporous Mesoporous Mater.*, 2002, **52**, 105–117.
30 J. I. Hayashi, A. Kazehaya, K. Muroyama and A. P. Watkinson, *Carbon*, 2000, **38**, 1873–1878.
31 C. Zhang, D. H. Liu, W. Lv, D. W. Wang, W. Wei, G. M. Zhou, S. G. Wang, F. Li, B. H. Li and F. Y. Kang, *et al.*, *Nanoscale*, 2015, **7**, 5592–5597.
32 H. Li, Y. Tao, X. Y. Zheng, J. Y. Luo, F. Y. Kang, H. M. Cheng and Q. H. Yang, *Energy Environ. Sci.*, 2016, **9**, 3135–3142.
33 M. Thommes, K. Kaneko, A. V. Neimark, J. P. Olivier, F. Rodriguez-Reinoso, J. Rouquerol and K. S. W. Sing, *Pure Appl. Chem.*, 2015, **87**, 1051–1069.
34 J. W. Han, C. Zhang, D. B. Kong, X. Z. He, J. Xiao, F. Q. Chen, Y. Tao, Y. Wan and Q. H. Yang, *Nano Energy*, 2020, **72**, 104729.
35 P. Li, H. Li, D. Han, T. Shang, Y. Deng, Y. Tao, W. Lv and Q.-H. Yang, *Adv. Sci.*, 2019, **6**, 1802355.
36 X. Liu, D. Lyu, C. Merlet, M. J. A. Leesmith, X. Hua, Z. Xu, C. P. Grey and A. C. Forse, *Science*, 2024, **384**, 321–325.
37 P. Liang, G. Z. Zhu, W. Z. Wang, C. L. Huang, S. C. Wu, J. W. Zhou, X. C. Zhou, Y. Wu, S. X. Wang and M. Y. Wang, *et al.*, *J. Am. Chem. Soc.*, 2025, **147**, 18541–18549.
38 P. Liang, G. Z. Zhu, C. L. Huang, Y. Y. Li, H. Sun, B. Yuan, S. C. Wu, J. C. Li, F. F. Wang and B. J. Hwang, *et al.*, *Adv. Mater.*, 2024, **36**, 2307192.

 This journal is © The Royal Society of Chemistry 2025